Quaternary Science Reviews 281 (2022) 107434

Contents lists available at ScienceDirect

Quaternary Science Reviews

journal homepage: www.elsevier.com/locate/quascirev

Paleoclimate reconstruction of the last 36 kyr based on branched glycerol dialkyl glycerol tetraethers in the Padul palaeolake record (Sierra Nevada, southern Iberian Peninsula)

Marta Rodrigo-Gámiz [a, *], Antonio García-Alix [a, b], Gonzalo Jiménez-Moreno [a], María J. Ramos-Román [c], Jon Camuera [c], Jaime L. Toney [d], Dirk Sachse [e], R. Scott Anderson [f], Jaap S. Sinninghe Damsté [g, h]

[a] Department of Stratigraphy and Paleontology, University of Granada, Spain
[b] Instituto Andaluz de Ciencias de la Tierra (IACT), CISC-UGR, Armilla, Spain
[c] Department of Geosciences and Geography, Faculty of Science, University of Helsinki, Finland
[d] School of Geographical and Earth Sciences, University of Glasgow, UK
[e] Helmholtz Centre Potsdam, German Research Centre for Geosciences GFZ, Section 5.1 Geomorphology, Organic Surface Geochemistry Lab., Germany
[f] School of Earth and Sustainability, Northern Arizona University, USA
[g] NIOZ Royal Netherlands Institute of Sea Research, Department of Marine Microbiology and Biogeochemistry, Den Burg, Texel, Netherlands
[h] Department of Earth Sciences, Faculty of Geosciences, Utrecht University, the Netherlands

ARTICLE INFO

Article history:
Received 3 November 2021
Received in revised form
11 February 2022
Accepted 20 February 2022
Available online 26 February 2022

Handling Editor: Yan Zhao

Keywords:
GDGTs distribution
Mean annual air temperature reconstruction
pH reconstruction
Continental sediment record
Southern Spain
Heinrich stadials
Dansgaard–Oeschger events

ABSTRACT

Quantitative continental climate reconstructions covering the last glacial cycle from the Iberian Peninsula are scarce. In order to fill this gap, we obtained for the first time a high-resolution mean annual air temperature (MAAT) record based on the distribution of specific bacterial membrane lipids (i.e., branched glycerol dialkyl glycerol tetraethers; brGDGTs) from the last 36.0–4.7 kyr palaeolake record recovered by the Padul-15-05 sedimentary core (Padul, Sierra Nevada, southern Iberia). The fractional abundance of the three major groups of GDGTs present in the Padul sediments, GDGT-0, crenarchaeol and the summed brGDGTs, is comparable with that of other shallow and small (<10 km^2) European lakes. Despite variations in the lithology in the studied section, the GDGT composition remains relatively stable, except for the uppermost 116 cm of the record, representing the ephemeral/emerged lake stage, which is characterized by higher crenarchaeol fractional abundances. The identification of a specific brGDGT that has only been detected in anoxic lakes provides evidence for *in-situ* brGDGT production in the water column and/or sediments in the Padul palaeolake. Its presence/absence probably denotes a succession of periods with a variable oxygen content in the bottom waters of the palaeolake. MAAT was reconstructed based on the distribution of brGDGTs using an African lake calibration and ranged between 12 and 20 °C. A new Bayesian calibration to mean temperature of Months Above Freezing (MAF) depicts similar temperature variations with a mean absolute difference of 0.7 °C. The MAAT reconstruction in the Padul palaeolake for the 36.0–4.7 kyr period reveals similarities with climate variability described at high-latitudes and in the westernmost Mediterranean area during this interval, showing cold conditions during the last three Heinrich Stadials and the Younger Dryas and warm conditions during the Dansgaard–Oeschger interstadials (7–1) and the Bölling-Alleröd period. Despite the more stable and warm general climate conditions during the Early and Mid-Holocene, rapid centennial-scale temperature changes are registered in the Padul palaeolake in good agreement with variations observed in the Mediterranean forest record.

1. Introduction

Paleoclimate studies aim to reconstruct past environmental conditions to better understand present and future climate

* Corresponding author.
E-mail address: martarodrigo@ugr.es (M. Rodrigo-Gámiz).

https://doi.org/10.1016/j.quascirev.2022.107434

variability. The reconstruction of past temperature oscillations is of especial interest as it reflects an important component of the present-day climate system (IPCC, 2021). The last glacial period (last 115 kyr), including the last deglaciation (last 18 to 11.6 kyr), with the present interglacial Holocene is the most recent time period when large global temperature changes occurred, amplified by changes in insolation and greenhouse gas concentrations (e.g., Shakun et al., 2012). During this time period, rapid and short-term climate variability occurred in the Northern Hemisphere, such as the Dansgaard/Oeschger (D/O) cycles (Bond et al., 1993; Dansgaard et al., 1993) and the transport of ice-rafted debris during Heinrich events related to cold temperature intervals in the North Atlantic defined as Heinrich Stadials (HS) (Heinrich, 1988; Hemming, 2004). The current interglacial Holocene, which started at about 11.7 kyr, is characterized by a generally more stable climate.

Continental paleotemperature reconstructions covering the last glacial termination in the Iberian Peninsula are scarce. The Padul basin (726 m a.s.l.), located at the foothill of Sierra Nevada in the southern Iberian Peninsula, presents one of the most expanded Pleistocene sedimentary sequence of the alternation of lacustrine and fen (called palaeolake hereafter) sediments in southern Europe, which has continuously recorded climate variability for the last ~200 kyr (Ortiz et al., 2004; Camuera et al., 2018, 2019, 2021; Ramos-Román et al., 2018a,b; Webster, 2018; García-Alix et al., 2021). Previous studies in the area have investigated vegetation and climate variability for the Pleistocene and Holocene periods mostly based on palynological and elemental geochemical proxies (del Río et al., 1992; Florschütz et al., 1971; Menéndez Amor and Florschütz, 1962, 1964; Ortiz et al., 2004, 2010; Pons and Reille, 1988; Ramos-Román et al., 2018a,b; Camuera et al., 2018, 2019, 2021; García-Alix et al., 2021), but no studies have focused on the reconstruction of past temperatures.

The distributions of glycerol dialkyl glycerol tetraethers (GDGTs), membrane lipids of bacteria and archaea that occur ubiquitously in a range of natural archives of both marine and continental environments, have been shown to be a promising temperature proxy (Schouten et al., 2013, and references therein). The two most common and abundant groups of GDGT lipids are isoprenoidal (iso) GDGTs, synthesized by a wide range of archaea (Schouten et al., 2013), and branched (br) GDGTs, produced by a few species of *Acidobacteria* but probably also by other groups of bacteria (cf., Sinninghe Damsté et al., 2018, and references therein). The brGDGTs are commonly more abundant than isoGDGTs in continental sedimentary environments such as soils and lake sediments (e.g., Schouten et al., 2013). The brGDGTs were discovered twenty years ago in a Dutch peat bog (Sinninghe Damsté et al., 2000), and since then, their distribution and response to different environmental changes have been an ongoing topic of research in paleoenvironmental studies. Despite the uncertainties in the source organisms of brGDGTs, their chemical structure and distribution have been shown to be influenced by environmental conditions, like continental air temperature and soil pH (Weijers et al., 2007a). In continental environments, their distribution, provenance, and response to environmental parameters has been investigated in different lakes (e.g., Powers et al., 2005; Tierney et al., 2010; Blaga et al., 2009; Niemann et al., 2012; Loomis et al., 2011, 2012, 2014a, 2014b; Woltering et al., 2014; Russell et al., 2018; Weber et al., 2018; Martin et al., 2019, 2020; Zhang et al., 2021; Zhao et al., 2021), soils (e.g., Weijers et al., 2007b; Peterse et al., 2012), rivers (Zell et al., 2014; Warden et al., 2016), peats (Sinninghe Damsté et al., 2000; Weijers et al., 2006; Naafs et al., 2017b), and other environments such as hot springs, fossil bones, and methane seeps (Li et al., 2014; Dillon et al., 2018; Zhang et al., 2020). In particular, the degree of methylation of brGDGTs (expressed by the MBT index) has been shown to vary with pH and mean annual air temperature (MAAT), whereas the degree of cyclization of branched tetraethers (expressed with the CBT index) varies with soil pH (Weijers et al., 2007a; Peterse et al., 2010). After the initial discovery of brGDGTs, improved analytical methods resulted in the recognition of 5-methyl and 6-methyl brGDGTs as major isomers (De Jonge et al., 2013). Importantly, the relative abundance of the 5-methyl isomers was determined to be more sensitive to temperature than pH, and De Jonge et al. (2014a) proposed modified versions of the MBT and CBT indices. In recent years, these indices have been used for a set of different calibrations depending on the kind of environment, including soil records (e.g., Peterse et al., 2012; De Jonge et al., 2014a; Naafs et al., 2017b), peats (e.g., Naafs et al., 2017a) and lake sediments (e.g., Russell et al., 2018). Recently, a new Bayesian calibration to determine the mean temperature of Months Above Freezing (MAF), based on the previous Bayesian approach BayMBT proposed by Dearing Crampton-Flood et al. (2020), has been introduced for lake sediments (Martínez Sosa et al., 2021).

Here we study for the first time the distribution of GDGTs in the sedimentary record of the Padul palaeolake with the aim to reconstruct quantitatively paleoenvironmental changes such as MAAT for a key time interval such as the last 36 kyr. Various GDGTs-based ratios have been used to evaluate their environmental sources in comparison with the previously obtained sedimentological and lithological changes, palynological data and geochemical analysis. In addition, the obtained MAAT record was compared with sea surface temperature variability observed in a marine record from the nearby westernmost Mediterranean Sea.

2. Material and methods

2.1. Sediment core, lithology and chronology

The Padul-15-05 sediment core (37°00′39.77″ N; 3°36′14.06″ W) with a length of 42.64 m, was collected in July 2015 at the edge of the present-day Padul lake (Fig. 1), which covers an area of ca. 4 km^2. The Padul basin is an enclosed and endorheic basin with groundwater inputs from different aquifers as main water source (Castillo Martín et al., 1984; Ortiz et al., 2004). Abundant and diverse plants, shrubs and herbs grow around the present-day lake and at the lake shore, providing an important input of terrestrial organic matter accumulated in the area. The current morphology and depth of the Padul lake (maximum of 14 m) is the result of the anthropogenic exploitation as peat quarry and does not reflect the natural situation. The Padul-15-05 core was recovered using a Rolatec RL-48-L drilling machine equipped with a hydraulic piston corer from the Scientific Instrumentation Center of the University of Granada (CIC-UGR, Spain). The core was split longitudinally and stored in a cool room at 4 °C in the Department of Stratigraphy and Paleontology at the University of Granada. One half of the core was sampled every 1 cm and split for different analyses. In this study, we focus on the uppermost 6.75 m of the Padul-15-05 sedimentary record.

The lithology of the Padul-15-05 core mainly consists of black clayey organic peat, hereafter referred as organic matter-rich (OM-rich) or “peat” sediments with intercalations of yellowish clayey-carbonate and carbonate facies. For the uppermost 6.75 m of the core, the lithology and facies are characterized by OM-rich or peat facies up to 5.98 m. Yellowish clayey-carbonate facies are present between 5.98 and 4.60 m depth, followed by a thin OM-rich layer from 4.60 to 4.20 m, and then by yellowish carbonate facies from 4.20 to 3.82 m (see details in Camuera et al., 2018). The OM-rich or peat facies are present between 3.82 and 1.16 m, followed by brown clay and carbonate facies for the topmost 1.16 m (described as Units 3 and 4; Ramos-Román et al., 2018b). The studied sedimentary section was previously interpreted to reflect a relatively shallow

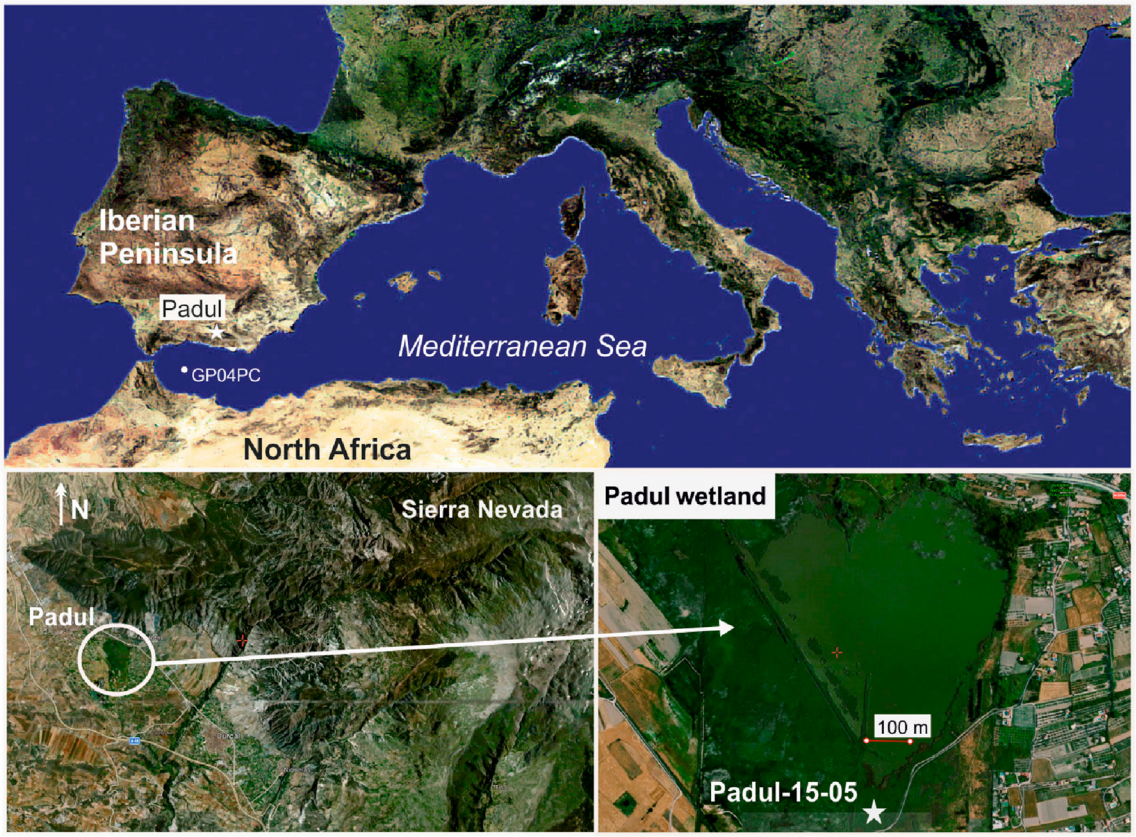

Fig. 1. Location and images of the present-day geomorphology and cover area of the Padul lake in the southern Iberian Peninsula. A zoom image in the Padul area shows the site (white star) of the recovered Padul-15-05 core. Images are from Google Earth (http://www.google.com/earth/index.html). The marine record GP04PC from the Alboran Sea in the westernmost Mediterranean (Morcillo-Montalbá et al., 2021) is included for comparison of the temperature records.

lake with a varying depth during the Late Pleistocene, ultimately lowering the lake level and even with ephemeral conditions for the Late Holocene (Camuera et al., 2018, 2019).

The age model of the uppermost 6.75 m of core Padul-15-05, corresponding to the last ~36 kyr, is based on 36 ^{14}C AMS radiocarbon dates (including 3 compound-specific radiocarbon dates), previously published by Ramos-Román et al. (2018a,b) and Camuera et al. (2018).

2.2. Biomarker extraction and GDGT analysis

For the GDGT analyses 1 cm thick slices of the sediment core were selected every 5 cm for the 36-12 kyr section, and every 10 cm for most of the Holocene section, except for the 5.7–4.7 kyr interval where sediment slices were selected every 5 cm. In total 93 samples were analysed. Total lipid extract (TLE) was extracted from ~1 cm^3 of sediment with an accelerated solvent extractor system Thermo Scientific™ Dionex™ ASE™ 350 using a mixture of dichloromethane:methanol (DCM:MeOH, 9:1, *v/v*). The TLE was separated by column chromatography using silica gel into apolar and polar fractions as described by Rach et al. (2020). Prior to analysis, each polar fraction was subdivided in two aliquots using DCM. One aliquot was dissolved in *n*-hexane:iso-propanol (99:1, *v/v*) and filtered through a 0.45 μm polytetrafluorethylene (PTFE) filter at the University of Granada. Filtered samples were analysed by ultra-high performance liquid chromatography/atmospheric pressure chemical ionization-mass spectrometry (UHPLC/APCI-MS) following the method described by Hopmans et al. (2016) and using a Waters Acquity UPLC I Class coupled to a Waters Xevo TQ-XS triple quadrupole mass spectrometer at CIC-University of Granada. Compounds were separated using two UHPLC silica columns (Waters BEH HILIC columns, 2.1 × 150 mm, 1.7 μm) fitted in series. Samples were eluted isocratically for 25 min with *n*-hexane:iso-propanol (98.2:1.8; *v/v*), followed by a linear gradient to *n*-hexane:iso-propanol (96.5:3.5; *v/v*) for 25 min, and then a linear gradient to *n*-hexane:iso-propanol (90:10; *v/v*) over 30 min, which was then maintained for 10 min. Flow rate was 0.2 mL per min and back pressure ranged from 200 to 230 bars. The total run time was 110 min, including 20 min for re-equilibration prior to the injection of the next sample. Various GDGTs (Fig. 2) were detected using selective ion monitoring (SIM) of the protonated molecules $[M + H]^+$ with Atmospheric Pressure Chemical Ionization (APCI) source conditions as in Schouten et al. (2007), at *m/z* 1302.2, 1300.2, 1298.2, 1296.2, 1292.2, 1050.0, 1048.0, 1046.0, 1036.0, 1034.0, 1032.0, 1022.0, 1020.0, 1018.0, and peak areas were determined using the MassLynx chromatography management's software, allowing automatic and manual integrations. The core top sample from the Padul-15-05 record was used as an external standard and run at the beginning and the end of each batch of samples to test the process reproducibility and to detect instrument drift.

2.3. GDGT ratios and proxies

We calculated several GDGTs-based ratios in order to evaluate their response to different environmental factors. Weijers et al. (2007b) introduced the MBT index to quantify the fractional abundances of tetramethylated brGDGTs (Ia-Ic) relative to tetramethylated, pentamethylated (IIa-IIc), and hexamethylated (IIIa-

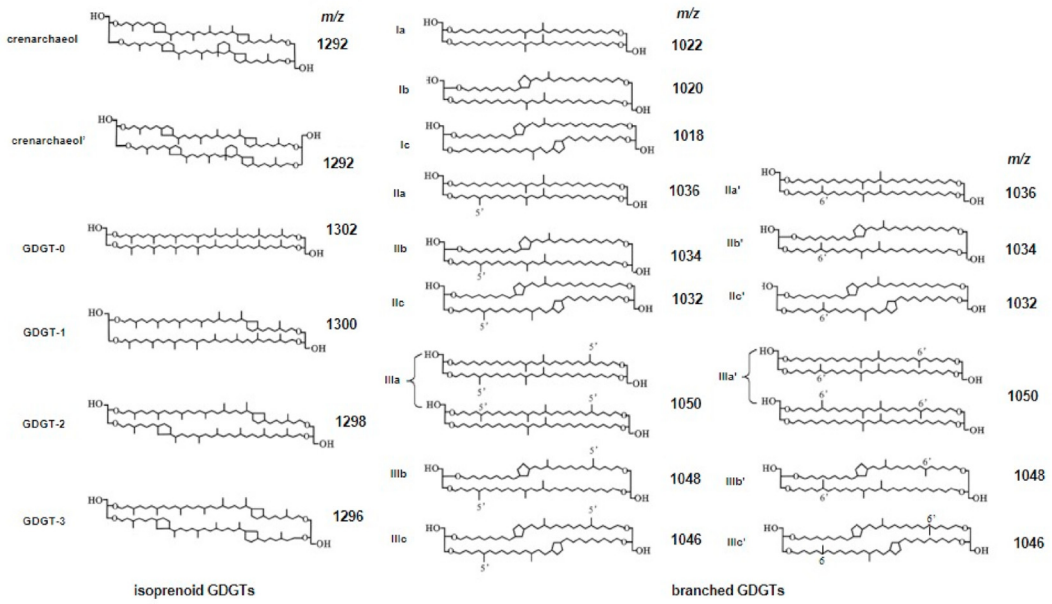

Fig. 2. Structures illustrate the main glycerol dialkyl glycerol tetraethers (GDGTs) identified in the Padul-15-05 sediment record, including crenarchaeol and its stereoisomer (Sinninghé Damsté et al., 2018), archaeal isoprenoidal (iso) and bacterial branched (br) GDGTs and *m/z* of the protonated molecules ($[M+H]^+$) identified by De Jonge et al. (2013) and Hopmans et al. (2016).

IIIc) compounds, which was further modified to the MBT' index by De Jonge et al. (2014a) including both the 5-methyl and 6-methyl isomers. De Jonge et al. (2014a) also defined a new MBT index (MBT'_{5ME}), where only the 5-methyl isomers were considered, which substantially improved the temperature calibration for soils:

$$MBT'_{5ME} = ([Ia] + [Ib] + [Ic]) / ([Ia] + [Ib] + [Ic] + [IIa] + [IIb] + [IIc] + [IIIa] + [IIIb] + [IIIc]) \quad (1)$$

Based on the CBT index proposed by Weijers et al. (2007b) for the cyclization of brGDGTs, De Jonge et al. (2014a) defined a new CBT' index:

$$CBT' = {}^{10}\log\{([Ic] + [IIa'] + [IIb'] + [IIc'] + [IIIa'] + [IIIb'] + [IIIc']) / ([Ia] + [IIa] + [IIIa])\} \quad (2)$$

The analytical reproducibility of theses indices was determined by running an external standard several times (n = 15), obtaining values of 0.006 for the MBT'_{5ME} index and 0.01 for the CBT' index.

To reconstruct mean annual air temperature (MAAT), we used two different calibrations:

the African lake calibration (Russell et al., 2018):

$$MAAT = -1.21 + 32.42 \text{ x } MBT'_{5ME} \ (n = 65, r^2 = 0.92; RMSE = 2.44\ ^\circ C) \quad (3)$$

where the analytical reproducibility (n = 15) was 0.2 °C.

and the Bayesian lake BayMBT calibration proposed by Martínez-Sosa et al. (2021) ($r^2 = 0.82$; RMSE = 2.9 °C), with a prior standard deviation (SD) set to 10 °C.

Lake water pH was reconstructed according to Russell et al. (2018) transfer function determined for East African lakes:

$$pH = 8.95 + 2.65 \text{ x } CBT' \ (n = 65; r^2 = 0.57; RMSE = 0.80) \quad (4)$$

Based on an uncommon hexamethylated brGDGTs, the IIIa'' isomer possessing one 5- and one 6-methyl substituent and eluting between the known 5- and 6-methyl hexamethylated brGDGT as described by Weber et al. (2015), we used the IIIa'' ratio which is defined as:

$$IIIa'' \text{ ratio} = [IIIa''] / ([IIIa] + [IIIa'] + [IIIa'']) \quad (5)$$

The relative abundance of the isomer of crenarchaeol was calculated as follows:

$$\%cren' = [cren'] / ([cren] + [cren']) \text{ x } 100 \quad (6)$$

The branched vs. isoprenoidal tetraether (BIT) index (Hopmans et al., 2004) reflects the relative abundance of the major bacterial brGDGTs vs. a specific archaeal isoGDGT, crenarchaeol (Fig. 1; Holzheimer et al., 2021), produced by Thaumarchaeota, with the inclusion of the 6-methyl brGDGTs (cf. De Jonge et al., 2013):

$$BIT = ([Ia] + [IIa] + [IIa'] + [IIIa] + [IIIa'])/ ([Ia] + [IIa] + [IIa'] + [IIIa] + [IIIa'] + [cren]) \quad (7)$$

3. Results

Both isoGDGTs and brGDGTs were detected in all the investigated sedimentary horizons of the Padul-15-05 record. However, the brGDGTs are dominant with abundances between 75 and 99.5%, as revealed by the ternary diagram (Fig. 3a), which also shows the relative abundances of GDGT-0 and crenarchaeol. The isomer of crenarchaeol (cren') was detected in trace amounts and was often below the detection limit at several intervals of the record (Fig. 5d). Crenarchaeol showed elevated abundances of 5–25% relative to all GDGTs in the first 116 cm of the record, characterized by brown clay and carbonate facies, associated with emerged conditions in the lake (Camuera et al., 2018, 2019). GDGT-0 was more abundant than crenarchaeol in all other facies, with relative abundances, sometimes slightly over 20%, especially in OM-rich facies (Fig. 3b). The average BIT index is 0.985 in the Padul-15-05 record.

The distribution of brGDGTs was dominated by penta- (IIa-c and

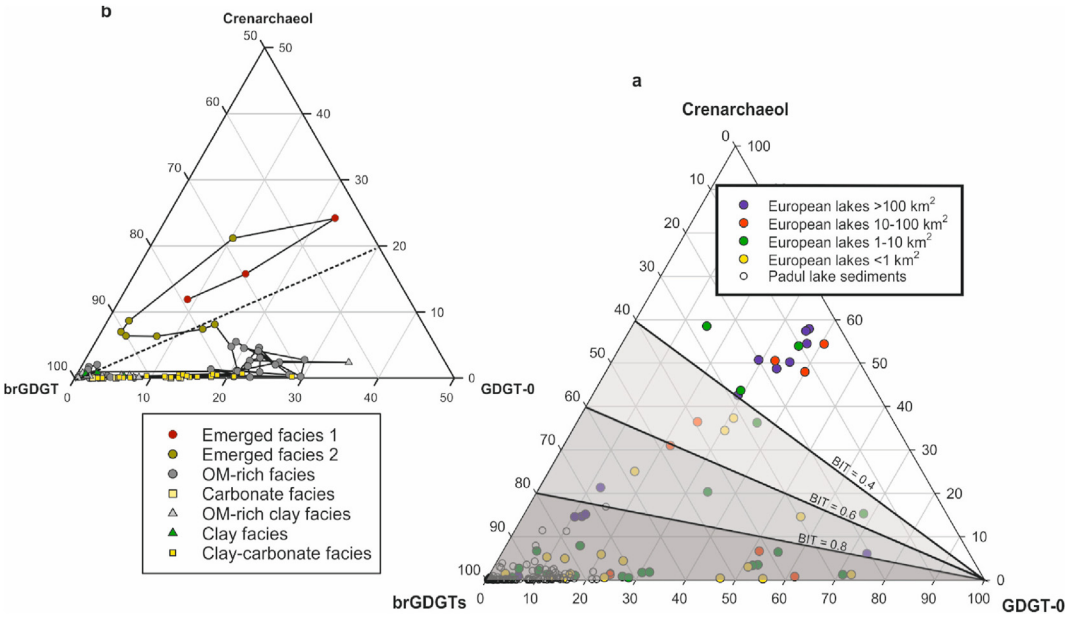

Fig. 3. (a) Ternary diagram (after Blaga et al., 2009) showing the composition of three major groups of GDGTs [i.e., GDGT-0, crenarchaeol (and its isomer cren') and the summed brGDGTs (with the exclusion of IIIa'')] in the Padul-15-05 sedimentary record indicated by the small white open circles. For reference, the same data is plotted for a set of surface sediments from 47 European lakes of a North-South transect (Blaga et al., 2009) and from 36 lakes from the Alpine area (Sinninghe Damsté et al., 2022). The area of the lakes is specified by the different, slightly larger, colored symbols. The increasing dark grey areas represent the increase in BIT values, showing that, in general, larger lakes and often deeper lakes have lower BIT values. (b) Magnification of the lower left corner of the ternary diagram showing in more detail the composition of the Padul palaeolake with the facies specified with different symbols. The solid black line connects the datapoints in a stratigraphic order starting with the three uppermost datapoints from the Padul-15-05 record. This shows that the sediments from the uppermost 116 cm described as brown clay and carbonate facies (Camuera et al., 2018) are characterized by higher creanarchaeol fractional abundances. For the remaining part of the section, there is no clear distinction in GDGT composition with the varying lithology and crenarchaeol fractional abundances are low. Dashed line indicates GDGT-0/crenarchaeol ratio of 2, whereas values higher than 2 correspond with GDGT-0 from other archaea than aquatic Thaumarchaeota, like methanogenic archaea. (For interpretation of the references to color in this figure legend, the reader is referred to the Web version of this article.)

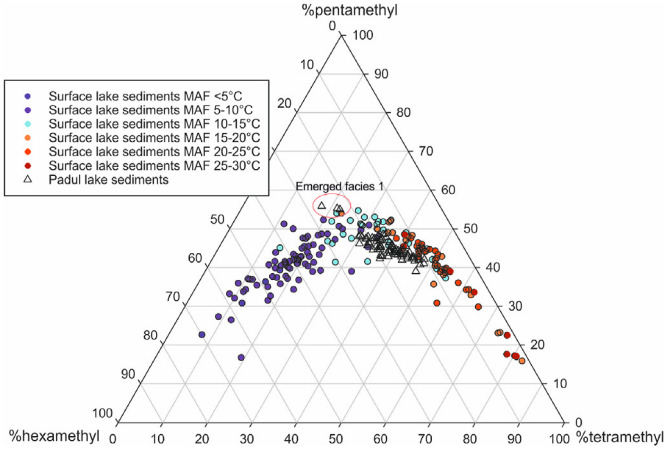

Fig. 4. Ternary diagram showing the composition of the brGDGTs in the Padul palaeolake sedimentary record (triangles). The tetramethylated brGDGTs are Ia-c, the pentamethylated IIa-IIc and IIa'-IIc', and the hexamethylated brGDGTs are IIIa-IIIc and IIIa'-IIIc'. The unusual brGDGT IIIa'' was excluded. For reference, comparable data from a variety of surface sediments of lakes from all over the world are plotted (circles). They are datasets published by Russell et al. (2018) on 64 African lakes, by Dang et al. (2018) on 36 Chinese lakes and Martínez-Sosa et al. (2021) on 106 globally distributed lakes. Lake Namso was excluded from the Chinese lake dataset because it has a highly unusual brGDGT distribution. The data points from the lake surface sediment set have been color-coded according to the mean temperature of months above freezing (MAF) as reported by Martínez-Sosa et al. (2021). The distribution of the datapoints of the Padul palaeolake sediments fit well to those of the surface lake sediments with MAFs in the range 15–20 °C except for the three uppermost datapoints from the Padul-15-05 record associated with emerged facies (Camuera et al., 2018), which distinctly lie outside the "Padul data cloud". (For interpretation of the references to color in this figure legend, the reader is referred to the Web version of this article.)

IIa'-IIc', between 50 and 70%) and tetramethylated (Ia-c, between 30 and 50%) brGDGTs, with much lower abundances of the hexamethylated brGDGTs (IIIa-c and IIIa'-IIIc', between 10 and 25%), throughout the entire record, except for the upper 33 cm of the section (equivalent to the last 800 cal yr BP), corresponding with emerged conditions (Camuera et al., 2018, 2019), where the hexamethylated are more abundant than the tetramethylated brGDGTs (Fig. 4).

The MBT'_{5ME} index ranges from 0.4 to 0.65, reaching the lower values at 644, 592, 531, 450–419, 280, and 226-215 cm (Fig. 5a) (equivalent to 33.1, 28.5, 22.2, 17.7–15.9, 9.3 and 7.5–7.2 cal kyr BP). The CBT' index varies from −0.54 to 0.28 in the record, with CBT' values generally below 0 from 675 to 382 cm (equivalent to 36–12.8 cal kyr BP), ranging from −0.20 to 0.10 from 376 to 122 cm (12.4–5.0 cal kyr BP), and positive values with an increasing trend for the upper 116 cm (last 4.7 cal kyr BP) (Fig. 5b).

In addition to the commonly observed brGDGTs, the hexamethylated brGDGT, which contains both a methyl at the 5- and the 6-positions of the two ether-bound alkyl chains (IIIa''), was detected as well. This brGDGT has so far only been reported in sediments of anoxic Swiss lakes and the anoxic water column of Lake Lugano (Weber et al., 2015, 2018). The IIIa'' ratio, which is based on the fractional abundance of IIIa'' over the sum fractional abundances of IIIa, IIIa'' and IIIa' [see Eq. (6)], varies between 0 and 0.10 (Fig. 5c). These data reveal variability between 0.05 and 0.10 at 592–547 and 387-116 cm (28.7–23.2 and 13.3–4.7 cal kyr BP), periods with rapid variability with values from 0 up to 0.10 at 659–644 and 460-392 cm (34.3–33.1 and 18.3–13.7 cal kyr BP), and periods with continuous absence of the IIIa'' isomer at 675–664, 638–598, 537–465, and the upper 106 cm of the record (Fig. 5c) (36.0–34.8, 32.7–29.1, 22.7–18.7 and last 4.6 cal kyr BP).

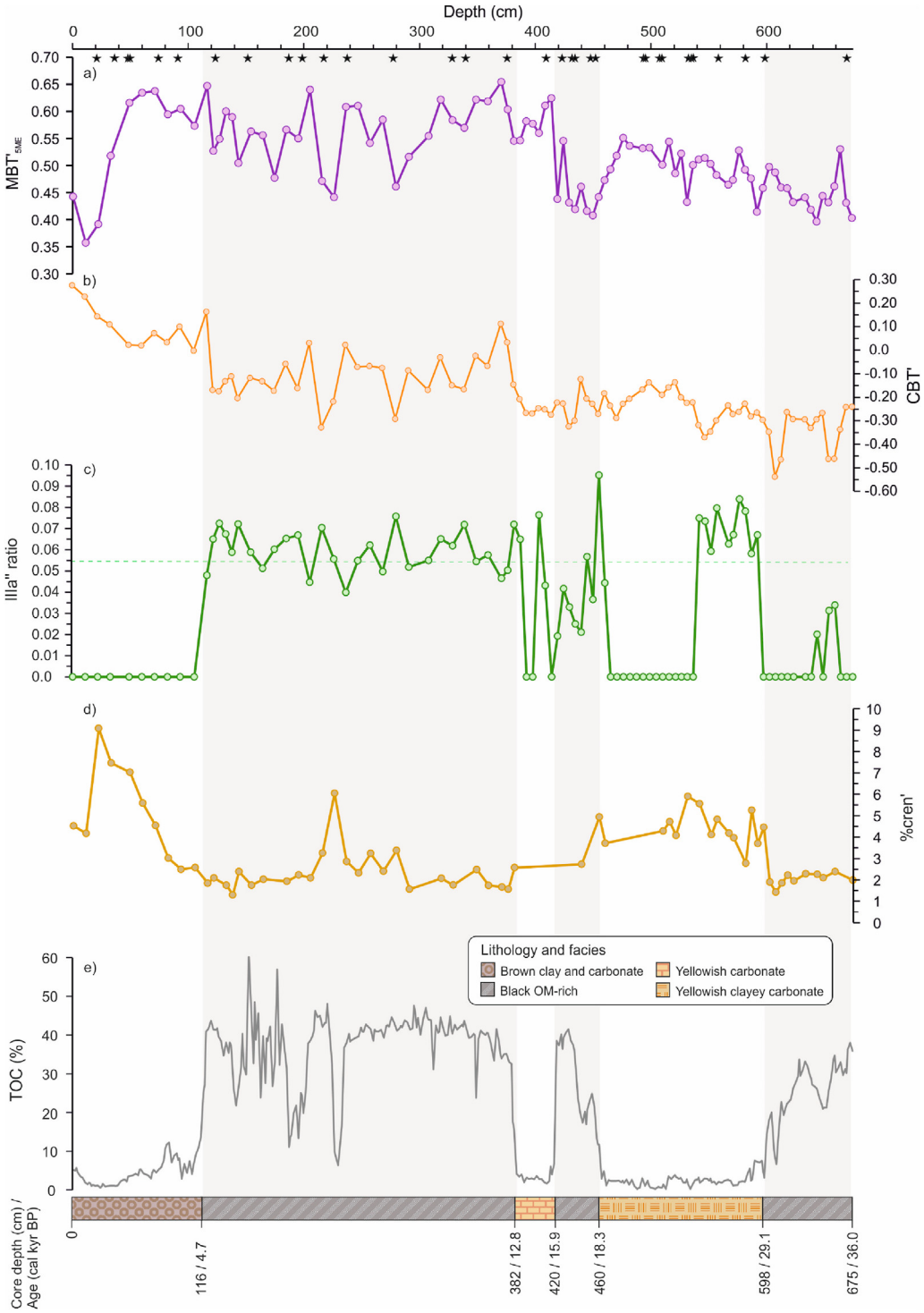

Fig. 5. Depth profile of the Padul palaeolake sedimentary record, Padul-15-05, showing: a) MBT'_{5ME}; b) CBT'; c) the IIIa'' ratio ([IIIa'']/[IIIa] + [IIIa''] + [IIIa']) based on the novel hexamethylated brGDGT described Weber et al. (2015); d) the %cren'; e) Total Organic Carbon (TOC) content (%) (Camuera et al., 2018). Bottom panel shows the different lithology and facies described for the upper 6.75 m depth (equivalent to the last 36 kyr) of the Padul-15-05 core (described by Ramos-Román et al., 2018b and Camuera et al., 2018). Vertical grey bars indicate periods with TOC content over 20%, coinciding with black OM-rich facies. Top stars indicate position of radiocarbon dates (for more details see Table 1 in Camuera et al., 2018). In all cases where the IIIa'' ratio is plotted as zero, IIIa'' was below the detection limit. In these cases, the IIIa'' ratio is always <0.005. It was often not possible to calculate %cren' because cren' was often below the detection limit and creanarchaeol abundance was also low. In these cases, no datapoint is shown.

4. Discussion

4.1. Distribution and sources of GDGTs in the Padul palaeolake

Previous studies have described significant lithological and sedimentological facies variations in the Padul-15-05 record, which have been related to changes in the water level, and hence to climate conditions (Ramos-Román et al., 2018a,b; Camuera et al., 2018, 2019). The clay-carbonate and carbonate facies with relatively low TOC values have been related to a high water level (Camuera et al., 2018, 2019) (Fig. 5e and bottom panel). In contrast, OM-rich facies are thought to have been deposited in a shallow palustrine (low water level) environment (Camuera et al., 2018, 2019) (Fig. 5e and bottom panel). Clay-OM-rich facies occur in the transition between OM-rich and clay-carbonate facies, when the water level was slightly higher than during OM-rich deposition, and with moderate TOC values (Fig. 5e and bottom panel) (Camuera et al., 2018, 2019). Lastly, for the upper 116 cm, low TOC values, similar to those during the yellowish clayey and carbonate facies, were identified (Fig. 5e). This section is characterized by brown clay and carbonate facies deposited in an ephemeral/dried lake stages preventing both very shallow palustrine sedimentation (OM-rich) and deeper lake level (carbonate) (Camuera et al., 2018, 2019). Therefore, most of the Padul-15-05 record was deposited in lake-type environmental conditions with substantial variability in the water level, except for the upper 116 cm of the record where a change towards ephemeral/emerged environment occurred (Ramos-Román et al., 2018a,b; Camuera et al., 2018, 2019).

These changes in sedimentological facies and environmental conditions during the sediment deposition in the Padul palaeolake may have resulted into a variable distribution and sources of GDGTs. However, when the variability of the GDGT distribution along the record is compared with lithological/facies changes and TOC content (Fig. 3a and b, 5e and bottom panel), this is not so evident. The BIT ratio is always >0.93 with an average of 0.99 (Fig. 3a, dark grey dashed area), indicating that overall brGDGTs are the dominant GDGTs in the Padul record. The BIT ratio has previously been thought to reflect the relative contributions of soil-vs. aquatic-derived GDGTs, assuming that brGDGTs were produced primarily in soils and isoGDGTs were derived primarily from the water column (e.g., Hopmans et al., 2004; Weijers et al., 2007b). Subsequent extensive studies on suspended particulate matter (SPM) in the water column of different lakes have shown that *in-situ* production in the water column of brGDGTs is rather common (e.g., Weber et al., 2018; van Bree et al., 2020). Thus, the high relative abundance of the brGDGTs relative to crenarchaeol and GDGT-0 does not exclude a lake depositional environment. Indeed, the GDGT distribution of many other European lakes are also located in the lower left corner of the ternary diagram (Fig. 3a). The low relative abundance of crenarchaeol contribution produced by Thaumarchaeota is similar to what is often observed in shallow and small (from <1 km^2 to up to 10 km^2) European lakes (Fig. 3a; see also Sinninghe Damsté et al., 2022).

Crenarchaeol indicates a Thaumarchaeotal source, while the other isoGDGTs could be produced by other archaea apart from Thaumarchaeota (Pancost et al., 2001; Schouten et al., 2013). Thus, a high GDGT-0/crenarchaeol ratio has been proposed to identify a contribution of isoGDGTs produced by methanogens (Blaga et al., 2009) or other Euryarchaeota (Schouten et al., 2013). This ratio is always >1, except for the upper 116 cm of the record, associated with ephemeral/dried lake conditions (Fig. 3b). This clearly suggests that other archaea than aquatic Thaumarchaeota were the major contributors of isoGDGTs for the deeper part of the Padul-15-05 record. In contrast, the relatively high abundance of crenarchaeol in the upper part of the Padul-15-05 record is likely due to a higher dominance of nitrifying Thaumarchaeota. Thaumarchaeota can be quite abundant in neutral to basic soils (Weijers et al., 2006; Peterse et al., 2010), in line with the idea that this part of the record reflects an ephemeral and dried-up lake. This is also supported by the higher abundance of cren' relative to crenarchaeol in the upper part of the record (Fig. 5d), since group 1.2 Thaumarchaeota that occur abundantly in soils also tend to have higher amounts of cren' (Sinninghe Damsté et al., 2012).

The evaluation of the different environmental sources of brGDGTs has been performed due to the improved chromatography method that allows to separate the 5- and 6-methyl isomers of the hexa- and pentamethylated brGDGTs (De Jonge et al., 2013; Hopmans et al., 2016). The distribution of the fractional abundance of the different hexa-, penta- and tetramethylated brGDGTs in the Padul palaeolake record are comparable with those recorded in a variety of surface lake sediments from 64 African lakes (Russell et al., 2018), 36 Chinese lakes (Dang et al., 2018), and 106 other globally distributed lakes (Martínez-Sosa et al., 2021). In this distribution, lake temperature plays an import role in determining the datapoint position in the ternary diagram (Fig. 4). The distribution of the brGDGTs in the upper part of the Padul-15-05 record (brown clay and carbonate facies) differs from those of the other sections, again pointing to a different (i.e., very shallow) depositional environment.

The presence of brGDGT IIIa'' also provides strong evidence of an *in-situ* brGDGT source in the water column (Fig. 5c). This brGDGT was identified for the first time in the sediments of an anoxic Swiss lake but not in the soils of the lake watershed, indicating *in-situ* production (Weber et al., 2015). Subsequently, IIIa'' was also identified in the sediments of other anoxic alpine (Weber et al., 2018) and French lakes (Martin et al., 2019, 2020). In a detailed study of the SPM in Lake Lugano, Weber et al. (2018) showed that IIIa'' exclusively occurred in the anoxic part of the water column, strongly suggesting that it is exclusively produced by anaerobic bacteria within the deep anoxic waters. The presence of the IIIa'' isomer (IIIa'' ratio >0; Fig. 5c), predominantly in the OM-rich intervals in the Padul record, indicates that, at that time of deposition, Padul was a lake with an oxycline within the water column, providing a niche for the bacteria that produce IIIa'' (cf., Weber et al., 2018). This supports the previously interpreted anoxic conditions for those sedimentary facies (Camuera et al., 2018). In line with the interpretation of the topmost brown clay and carbonate facies associated with an emerged palaeolake, IIIa'' was not detected in the upper part (0–106 cm) of the core (Fig. 5c), corresponding to the last 4.6 cal kyr BP. On the other hand, the IIIa'' ratio profile also shows older intervals where the IIIa'' isomer was below detection limit, i.e., at 675–664, 638–598, and 537-465 cm (36.0–34.8, 32.7–29.1, 22.7–18.7 cal kyr BP), and some intervals of rapid variability at 659–644 and 460-392 cm (34.3–33.1 and 18.3–13.7). These likely represent periods with an absence of an oxycline in the water column and periods where the depth of the oxycline varies, respectively. The intervals with quite stable IIIa'' ratios, i.e., at 592-547 cm and 387-116 cm (Fig. 5c) (28.5–23.2 and 13.3–4.7 cal kyr BP), indicate a stable oxycline in the water column of the lake.

In summary, the GDGT distribution in the Padul-15-05 sedimentary record is fully consistent with a small lake environment with substantial contribution of *in-situ* production of brGDGTs, except for the upper 116 cm of the record, when the lake likely became very shallow and subsequently dried up (i.e., an ephemeral/emerged environment).

4.2. Applicability of brGDGT-based proxies

The distribution of brGDGTs has been demonstrated to change

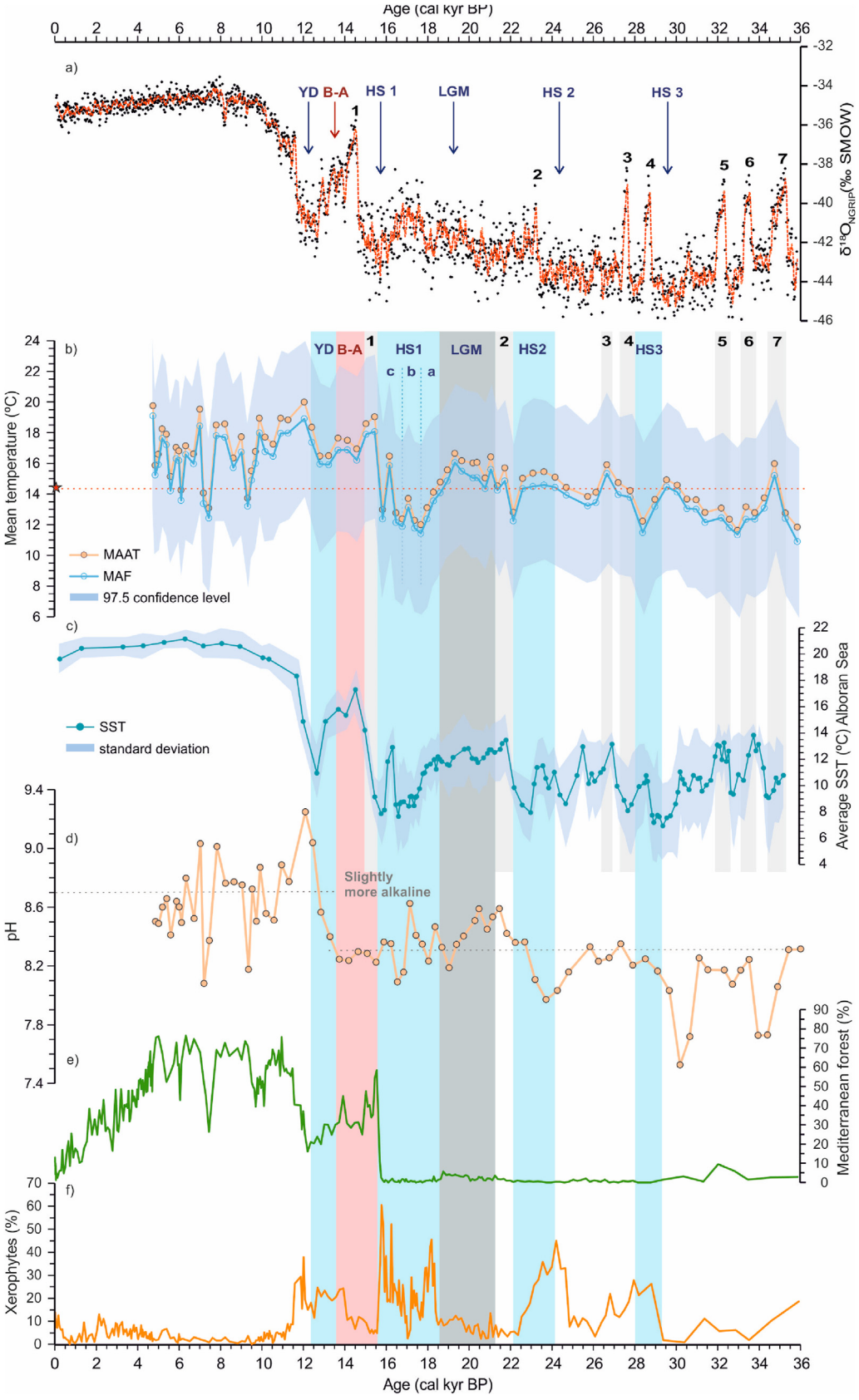

Fig. 6. BrGDGT based proxies and derived mean temperature from the Padul-15-05 sediment core for the last 36 kyr. a) The $\delta^{18}O$ profile of Greenland NGRIP ice core (data points are black circles and the dashed red line is the 5-points running mean) (Andersen et al., 2006; Svensson et al., 2008); b) Mean Annual Air Temperature (MAAT) (in °C) derived from MBT'_{5ME} using the lake calibration proposed by Russell et al. (2018) (orange-colored circles), and mean temperature of Months Above Freezing (MAF) (blue open circles) with the 97.5% confidence level bands (light blue band) based on the Bayesian lake calibration proposed by sediments Martínez Sosa et al. (2021). Red star and dashed line indicate mean

in response to both, temperature and pH (Weijers et al., 2007; Tierney and Russell, 2009; De Jonge et al., 2014b) and specific GDGT ratios have been proposed to reconstruct these environmental parameters. The chromatographic separation of the 5- and 6-methyl brGDGTs has allowed the improvement of the two initial defined indices—methylation index of branched tetraethers (MBT) and the cyclization index of branched tetraethers (CBT)—as MBT'_{5ME}, excluding the 6-methyl isomers, and CBT', which includes the 6-methyl isomers (De Jonge et al., 2014a).

An MBT'_{5ME}-based lacustrine calibration for reconstructing mean annual air temperatures (MAAT) was proposed by Russell et al. (2018) based on a large set of African lakes from different altitudes. This calibration accounts that lake temperatures should regulate the distribution of brGDGTs produced *in-situ* in the water column. When we apply this calibration to the Padul-15-05 dataset, excluding the uppermost section representing the emerged-ephemeral lake phase (brown clay and carbonate facies), reconstructed MAAT ranges between 12 and 20 °C (Fig. 6b). Recently, a Bayesian calibration has been constructed by Martínez-Sosa et al. (2021) based on the dataset of Russell et al. (2018), some Chinese and ca. 100 American lakes. This calibration used Months Above Freezing temperatures (MAF) instead of MAAT because colder lakes from high latitudes fitted better in the calibration due to a seasonally-biased response in the production of brGDGTs. The application of this latter Bayesian calibration generated estimated temperature that only differ from the MAAT estimation using the Russell et al. (2018) calibration by 0.2–1.2 °C (Fig. 6b). The Bayesian calibration also allows to make an estimation of the error in the MAF prediction; this is indicated by the light blue area at the 97.5% confidence level in Fig. 6b. Mean present-day annual temperature in the Padul area is 14.4 °C (Spanish National Weather Agency - AEMet Open Data, 2020; www.aemet.es), which is within the temperature range obtained by both lake calibrations (within the calibration error of 2.4 °C; Russell et al., 2018) and the Bayesian calibration (withing the calibration error of 2.9 °C; Martínez-Sosa et al., 2021). Therefore, both calibrations are deemed suitable for reconstructing lake temperatures in the Padul-15-05 record, and we will be referred to as MAAT values in the next section, since we do not have evidence of a seasonal-bias in the production of brGDGTs in the Padul palaeolake.

The CBT' values allowed to estimate palaeo pH using a recent lake-pH calibration (Russell et al., 2018) and showed that pH values ranged between 7.5 and 9.3, with an average of 8.4 (Fig. 6d). Interestingly, in the upper part of the Padul-15-05 record corresponding to the Holocene period, pH oscillates in parallel with MAAT variability (Fig. 6d), in contrast to the bottom part of the record corresponding to the last glaciation, suggesting that lake pH seems to play an important role in controlling the brGDGTs distribution during the Holocene. The pH profile at the onset of the Holocene shows a trend of generally more alkaline surface waters with an average value of 8.8 (Fig. 6d). Alkaline pH values of the lake are in line with the presence of *Botryococcus* remains (Camuera et al., 2019), which could indicate an increase in aquatic photosynthetic organisms and productivity.

4.3. Temperature reconstruction from 36 kyr to the mid-holocene

For the first time, we obtained a continuous and quantitative MAAT record from the southern Iberian Peninsula covering the last 36 kyr. Estimated MAAT values in the Padul-15-05 record using the lake calibration of Russell et al. (2018) range between 12 and 20 °C for the last 36–4.7 kyr, with the lowest MAAT values recorded during the HS1, followed by HS3 and HS2, with 12, 12.2 and 12.8 °C, respectively (Fig. 6b). Cold conditions likely caused a decrease in evapotranspiration, resulting in a high water level in Padul palaeolake (Camuera et al., 2018). High lake level periods in the Padul palaeolake in turn coincided with low Mediterranean forest abundance, represented by terrestrial pollen taxa more adapted to humid conditions, in the nearby Sierra Nevada and Padul area and enhancements of detrital inputs pointing to arid periods and enhanced erosion (Camuera et al., 2018, 2019). These environmental changes especially occurred in the Padul palaeolake during the last three Heinrich Stadials (HS3-1) recorded in the last 36 kyr (see Fig. 8 in Camuera et al., 2019). In addition, yellowish clayey and carbonate facies have been associated with highest lake level and coldest conditions in the Padul record, and further related to minima in summer insolation during MIS 2 (Camuera et al., 2018). Furthermore, the similarity of the MAAT and MAF records further support that the Padul palaeolake did not become frozen during the glacial and the three HS events.

A comparison of the MAAT estimations from the Padul-15-05 record with the paleoclimate variability recorded in the $\delta^{18}O$ NGRIP Greenland ice-record (Andersen et al., 2006; Svensson et al., 2008), and a recent study applying organic-based paleothermometers in a marine record GP04PC from the Alboran Sea in the westernmost Mediterranean (Morcillo-Montalbá et al., 2021), depict strong similarities in the temperature variability (Fig. 6a–c). Particularly, similar variability trends can be observed during the D/O interstadials 7 and 3, the last three HS (HS3-HS1) and the LGM between the MAAT in the Padul palaeolake and the average temperature derived from four organic proxies from the Alboran Sea record (Morcillo-Montalbá et al., 2021) (Fig. 6b–c). This supports a strong sea-land climatic coupling, although the temperature amplitude in the ocean appears to be higher than at the continent. Overall increased temperature values in the Padul palaeolake are recorded during the D/O interstadials and similar to those during the LGM, while decreasing temperatures are evident at the end of the HS3 and HS2 (Fig. 6b–c). The temperature amplitude changes during HS3 and HS2 are ca. 2.8 °C, and from the LGM to the onset of HS1 are ca. 4 °C (Fig. 6c).

Slight time shifts in the onset and offset of main climate periods are observed between the Padul-15-05 record and the nearby western Mediterranean marine record and the Greenland ice-core record (Fig. 6a–c). For instance, HS3 and HS2 appear to be delayed with respect to Greenland NGRIP and the western Mediterranean records, while HS1 presents an earlier onset and larger duration (Fig. 6a–c). This mismatch could be explained by different time response between lacustrine, marine and ice-core climate records, registering time shifts and different amplitude in temperature changes to the same climate variability. Some larger and lagged temperature changes may be also partly related to uncertainties in the radiocarbon-based age model from the different

present-day MAAT of 14.4 °C at Padul area (www.aemet.es); c) Sea surface temperature (SST) from the average of four organic-based proxies ($U^{K'}_{37}$, TEX^{H}_{86}, RI-OH' and LDI) from core GP04PC spanning the last 35.2 kyr from the Alboran Sea basin (Morcillo-Montalbá et al., 2021), whereas light blue band indicates standard deviation (+SD and -SD) of the four proxy-SST estimations; d) palaeo pH derived using the lake calibration proposed by Russell et al. (2018); e) Mediterranean forest pollen percentages including *Pinus* with respect to the total terrestrial pollen from Padul-15-05 (Camuera et al., 2019); f) Xerophytes percentages with respect to the total terrestrial pollen from Padul-15-05 (Camuera et al., 2019). Vertical blue bars indicate main cold periods for the last 36 kyr, i.e., the last three Heinrich Stadials (HS3, HS2, and HS1), the Younger-Dryas (YD). The dark grey vertical bar indicates the Last Glacial Maximum (LGM), the light red bar indicates the Bölling-Alleröd (B–A) event, and the light grey vertical bars indicate the Dansgaard-Oeschger (D/O) interstadials (7–1) (Bond et al., 1993; Dansgaard et al., 1993). (For interpretation of the references to color in this figure legend, the reader is referred to the Web version of this article.)

climate records (Camuera et al., 2021). Moreover, the enhanced freshwater discharges from the Laurentide and European ice-sheets at ~18.2 cal kyr BP (Toucanne et al., 2015) and the meltwater input from glaciers in the Alps and Apennines produced the first freshwater input to the western Mediterranean, which could have led to the slowdown of the Mediterranean Sea overturning circulation that has been registered with shifts in marine records (Rogerson et al., 2008).

Three main centennial-scale climate phases, HS1a-c, previously described in the Padul-15-05 record by Camuera et al. (2021), are also clearly revealed by the MAAT profile, despite its lower resolution (Fig. 6b). HS1a (18.4–17.2 cal kyr BP) is characterized by a low MAAT (12 °C; Fig. 6b), and a high percentage of the xerophytes group, which includes plants such as *Artemisia, Ephedra,* and Amaranthaceae adapted to dry environments (Fig. 6f). HS1b (17.2–16.9 cal kyr BP) is characterized by a slight increase in MAAT (up to 16.5 °C; Fig. 6b), and a decrease in the xerophytes abundance (Fig. 6f). HS1c (16.9–15.7 cal ka BP) is again characterized by a low MAAT (12.2 °C; Fig. 6b) and arid conditions, as reflected by the high percentage of the xerophytes (Fig. 6f). A similar temperature variability during HS1 has been recorded by the $\delta^{18}O$ NGRIP (Fig. 6a) and the Alboran (Fig. 6c) records, supporting the strong climate connection between mid- and high-latitudes and the high sensitivity of this continental southern Iberian record.

A noticeable increase in MAAT values is recorded from the HS1 to the onset of the B-A period (up to 18.6 °C; Fig. 6b), synchronously with changes in the pollen record (Camuera et al., 2019); i.e., an increase in Mediterranean forest taxa, which includes *Quercus* total, *Olea*, *Phillyrea*, *Pistacia, Cistaceae* and *Pinus* (Fig. 6e), and a decrease in the xerophytes taxa (Fig. 6e–f), also indicating an increase in temperature and humidity. Predominant carbonate sedimentation occurred during the B-A period (see bottom panel in Fig. 5), which was related to enhanced precipitation and low erosion, and hence low siliciclastic detrital input, due to an increase in the vegetation cover (Camuera et al., 2018, 2021; García-Alix et al., 2021). Other Mediterranean records have also documented general humid conditions during this period with high detrital input to the Alboran Sea basin (Rodrigo-Gámiz et al., 2011). Furthermore, the MAAT record suggested some climate sub-phases during the B-A period in agreement with recent palynological studies in the Padul record (Camuera et al., 2021), describing five centennial-scale pollen zones dominated by varying temperature and humid conditions.

Low MAAT values (16.4 °C) characterized the YD, with values ca. 0.5 °C lower than those recorded at the end of the B-A period (Fig. 6b). This small temperature change is in agreement with other studies in the southern Iberian describing only small climate changes for the YD stage (Naughton et al., 2016). Despite the small temperature amplitude change recorded from the B-A to the YD transition of ca. 1 °C, an increase in the arid conditions is also evident from the increase in the percentages of xerophytes and the decrease in the Mediterranean forest (Fig. 6e–f). An increasing trend in MAAT followed then into the Holocene. The increase in evapotranspiration that occurred due to highest summer insolation resulted in a low lake level in Padul palaeolake during the Holocene period (Camuera et al., 2018).

During the Early and Mid-Holocene, the Padul-15-05 MAAT record shows some rapid centennial-millennial scale variability, with a noticeable temperature amplitude in comparison with the deglaciation (Fig. 6b). Sedimentation during the Holocene is mostly characterized by black OM-rich facies with the highest TOC content, highest abundance of Mediterranean forest (60–80%; Fig. 6e) and interpreted as deposited during low lake levels (Fig. 5e and bottom panels) and related to warm and humid conditions (Camuera et al., 2018). Probably, the change in the environmental conditions during the Holocene amplified the temperature sensitivity of the Padul palaeolake. Previous palynological analysis of the Padul palaeolake section documented the highest occurrence of deciduous forest in the Padul area from ~9.5 to 7.6 cal kyr BP related to the Holocene humidity optimum and the highest precipitation recorded (García-Alix et al., 2021), coinciding with insolation maxima. More arid conditions are described from 7.6 to 4.7 cal kyr BP and related with a decrease in summer insolation that triggered an aridification process (Ramos-Román et al., 2018b). Nevertheless, millennial-scale variability with forest declines is observed around 9.6, 8.5, 7.5, 6.5 and 5.4, 4.7–4, 2.7 and 1.3 cal kyr BP (Ramos-Román et al., 2018b). The MAAT record suggests that some of these periods of Mediterranean forest decline in this area may also have been triggered by colder conditions (Fig. 6b, e), i.e., with a rapid temperature decrease from 19–18 °C to 13 °C at ~9.3, 7.4 and 6.1 cal ka BP (Fig. 6b). This rapid variability in the pollen and temperature records indicates a fast and sensitive environmental response to regional Holocene climate variability in the Padul palaeolake area.

5. Conclusions

For the first time, GDGTs distribution were examined in a sedimentary section covering the last 36 kyr in the Padul area (Sierra Nevada, southern Iberia). The generally high abundance of brGDGTs relative to crenarchaeol and GDGT-0 points to lake-type environmental conditions with substantial variability in the water level, except for the upper part of the Padul-15-05 record, which shows a change in the distribution toward an emerged-ephemeral lake environment. The presence of brGDGT IIIa'' provided strong evidence for *in-situ* brGDGT production in the water column of the palaeolake, and its distribution along the record indicates variations in the depth of the oxycline.

The Padul record of the MBT'_{5ME} index in combination with the lake calibration of Russell et al. (2018) revealed MAATs ranging between 12 and 20 °C for the last 36–4.7 kyr. Application of a recent Bayesian calibration (Martínez-Sosa et al., 2021) showed that estimations for MAF only differ from the MAAT estimations by 0.2–1.2 °C. Millennial-scale MAAT variability is recorded in the Padul palaeolake, with lower temperature values during the last three Heinrich Stadials (HS3-1), and higher temperature values during the D/O interstadials, the LGM and the Holocene. This temperature variability is comparable to that recorded in the $\delta^{18}O$ NGRIP Greenland ice-record and marine sedimentary records from the westernmost Mediterranean (Alboran Sea), supporting the strong climate connection between mid- and high-latitudes and the high sensitivity of this continental southern Iberian record with the continental and marine teleconnection.

Author contribution

The individual contributions have been: M. Rodrigo-Gámiz have performed the GDGTs analysis, interpreted the data and wrote the manuscript. A. García-Alix, G. Jiménez-Moreno and R.S. Anderson contributed to the writing of the manuscript. A. García-Alix, M.R. Ramos-Román, J. Camuera, J.L. Toney, and D. Sachse performed the sample extractions. J.S. Sinninghe Damsté discussed data and interpretations and wrote the manuscript.

Declaration of competing interest

The authors declare that they have no known competing financial interests or personal relationships that could have appeared to influence the work reported in this paper.

Acknowledgments

This research was supported by Projects CGL2013- 47038-R and CGL2017-85415-R funded by Ministerio de Economia y Competitividad, Secretaria de Estado de Investigacion, Desarrollo e Innovacion, I+D+i (Spain), Project IE2017-5534 from Ayudas a infraestructuras y equipamientos de I+D+i, Plan Andaluz de Investigación, Desarrollo e Innovación (PAIDI 2020), Grants FEDER/Junta de Andalucía-Consejería de Economía y Conocimiento B-RNM-144-UGR18, A-RNM-336-UGR20 and P20_00059, and Research Group RNM-190 (Junta de Andalucía, Spain). M.R.G. acknowledges post-doctoral fellowship Juan de la Cierva-Incorporación program (IJCI-2017-33755) from Secretaría de Estado de I+D+i (Spain), and funds received by the program "Ayudas para la utilización del CIC" del Plan Propio de Investigación y Transferencia 2019 of the University of Granada. A.G.-A.D. acknowledges funding from the Ramon y Cajal program (RYC-2015-18966) from Secretaría de Estado de I+D+i (Spain). M.J.R.R. acknowledges post-doctoral funding (ERC-2017-ADG-788616). J.S.S.D. receives support by the Netherlands Earth System Science Centre (NESSC) Gravitation Grant (024.002.001) of the Netherlands Ministry of Education, Culture and Science (OCW) and the Netherlands Organization for Scientific Research (NWO). We thank Ellen C. Hopmans and Denise Dorhout from NIOZ for their help and comments on the implementation of the UPLC-MS method at CIC-University of Granada. We are also grateful to Samuel Cantarero from the Centre for Scientific Instrumentation (CIC, Spain) for the analyses and support at the UHPLC-MS. We acknowledge Pablo Martínez-Sosa for his help with the Bayesian calibration estimation. We thank the Associate Editor, Dr. Yan Zhao and two anonymous reviewers, for their helpful comments that improved the manuscript. Funding for open access charge from Universidad de Granada/CBUA.

Appendix A. Supplementary data

Supplementary data to this article can be found online at https://doi.org/10.1016/j.quascirev.2022.107434.

Dataset presented in this study is available in the open-access repository Zenodo. https://doi.org/10.5281/zenodo.5643130.

References

Andersen, K.K., Svensson, A., Johnsen, S.J., Rasmussen, S.O., Bigler, M., Röthlisberger, R., Ruth, U., Siggaard-Andersen, M.-L., Steffensen, J.P., Dahl-Jensen, D., Vinther, B.M., Clausen, H.B., 2006. The Greenland ice core chronology 2005, 15-42 ka. Part 1: constructing the time scale. Quat. Sci. Rev. 25, 3246–3257. https://doi.org/10.1016/j.quascirev.2006.08.002.

Blaga, C.I., Reichart, G.J., Heiri, O., Sinninghe Damsté, J.S., 2009. Tetraether membrane lipid distributions in lake particulate matter and sediments: a study of 47 European lakes along a North–South transect. J. Paleolimnol. 41, 523–540. https://doi.org/10.1007/s10933-008-9242-2.

Bond, G., Broecker, W., Johnsen, S., McManus, J., Labeyrie, L., Jouzel, J., Bonani, G., 1993. Correlations between climate records from North Atlantic sediments and Greenland ice. Nature 365, 143–147. https://doi.org/10.1038/365143a0.

Camuera, J., Jiménez-Moreno, G., Ramos-Román, M.J., García-Alix, A., Toney, J.L., Anderson, R.S., Jiménez-Espejo, F., Kaufman, D., Bright, J., Webster, C., Yanes, Y., Carrión, J.S., Ohkouchi, N., Suga, H., Yamame, M., Yokoyama, Y., Martínez-Ruiz, F., 2018. Orbital-scale environmental and climatic changes recorded in a new ~ 200,000-year-long multiproxy sedimentary record from Padul, southern Iberian Peninsula. Quat. Sci. Rev. 198, 91–114. https://doi.org/10.1016/j.quascirev.2018.08.014.

Camuera, J., Jiménez-Moreno, G., Ramos-Román, M.J., García-Alix, A., Toney, J.L., Anderson, R.S., Jiménez-Espejo, F., Bright, J., Webster, C., Yanes, Y., Carrión, J.S., 2019. Vegetation and climate changes during the last two glacial-interglacial cycles in the western Mediterranean: a new long pollen record from Padul (southern Iberian Peninsula). Quat. Sci. Rev. 205, 86–105. https://doi.org/10.1016/j.quascirev.2018.12.013.

Camuera, J., Jiménez-Moreno, G., Ramos-Román, M.J., García-Alix, A., Jiménez-Espejo, F., Toney, J.L., Anderson, R.S., 2021. Chronological control and centennial-scale climatic subdivisions of the Last Glacial Termination in the western Mediterranean region. Quat. Sci. Rev. 255, 106814. https://doi.org/10.1016/j.quascirev.2021.106814.

Castillo Martín, A., Benavente Herrera, J., Fernández Rubio, R., Pulido Bosch, A., 1984. Evolución y ámbito hidrogeológico de la laguna de Padul (Granada), Las Zonas Húmedas en Andal. Monogr. DGMA-MOPU.

Dang, X., Ding, W., Yang, H., Pancost, R.D., Naafs, B.D.A., Xue, J., Lin, X., Lu, J., Xie, S., 2018. Different temperature dependence of the bacterial brGDGT isomers in 35 Chinese lake sediments compared to that in soils. Org. Geochem. 119, 72–79. https://doi.org/10.1016/j.orggeochem.2018.02.008.

Dansgaard, W., Johnsen, S.J., Clausen, H.B., Dahl-Jensen, D., Gundestrup, N.S., Hammer, C.U., Hvidberg, C.S., Steffensen, J.P., Sveinbjörnsdottir, A.E., Jouzel, J., Bond, G., 1993. Evidence for general instability of past climate from a 250-kyr ice-core record. Nature 364, 218–220. https://doi.org/10.1038/364218a0.

Dearing Crampton-Flood, E., Tierney, J.E., Peterse, F., Kirkels, F.M., Sinninghe Damsté, J.S., 2020. BayMBT: a Bayesian calibration model for branched glycerol dialkyl glycerol tetraethers in soils and peats. Geochem. Cosmochim. Acta 268, 142–159. https://doi.org/10.1016/j.gca.2019.09.043.

De Jonge, C., Hopmans, E.C., Stadnitskaia, A., Rijpstra, W.I.C., Hofland, R., Tegelaar, E., Sinninghe Damsté, J.S., 2013. Identification of novel penta- and hexamethylated branched glycerol dialkyl glycerol tetraethers in peat using HPLC–MS^2, GC–MS and GC–SMB-MS. Org. Geochem. 54, 78–82. https://doi.org/10.1016/j.orggeochem.2012.10.004.

De Jonge, C., Hopmans, E.C., Zell, C.I., Kim, J.-H., Schouten, S., Sinninghe Damsté, J.S., 2014a. Occurrence and abundance of 6-methyl branched glycerol dialkyl glycerol tetraethers in soils: implications for palaeoclimate reconstruction. Geochem. Cosmochim. Acta 141, 97–112. https://doi.org/10.1016/j.gca.2014.06.013.

De Jonge, C., Stadnitskaia, A., Hopmans, E.C., Cherkashov, G., Fedotov, A., Sinninghe Damsté, J.S., 2014b. In situ produced branched glycerol dialkyl glycerol tetraethers in suspended particulate matter from the Yenisei River, Eastern Siberia. Geochem. Cosmochim. Acta 125, 476–491. https://doi.org/10.1016/j.gca.2013.10.031.

del Río, J.C., Gónzalez-Vila, F.J., Martin, F., 1992. Variation in the content and distribution of biomarkers in two closely situated peat and lignite deposits. Org. Geochem. 18, 67–78.

Dillon, J.T., Lash, S., Zhao, J., Smith, K.P., van Dommelen, P., Scherer, A.K., Huang, Y., 2018. Bacterial tetraether lipids in ancient bones record past climate conditions at the time of disposal. J. Archaeol. Sci. 96, 45–56. https://doi.org/10.1016/j.jas.2018.05.009.

Florschütz, F., Menéndez Amor, J., Wijmstra, T.A., 1971. Palinology of a thick Quaternary succession in southern Spain. Palaeogeogr. Palaeoclimatol. Palaeoecol. 10, 233–264.

García-Alix, A., Camuera, J., Ramos-Román, M.J., Toney, J.L., Sachse, D., Schefuss, E., Jiménez-Moreno, G., Jiménez-Espejo, F.J., López-Avilés, A., Anderson, R.S., Yanes, Y., 2021. Paleohydrological dynamics in the Western Mediterranean during the last glacial cycle. Global Planet. Change 202, 103527. https://doi.org/10.1016/j.gloplacha.2021.103527.

Heinrich, H., 1988. Origin and consequences of cyclic ice rafting in the northeast Atlantic Ocean during the past 130,000 years. Quaternary Research 29, 142–152. https://doi.org/10.1016/0033-5894(88)90057-9.

Hemming, S.R., 2004. Heinrich events: massive late Pleistocene detritus layers of the North Atlantic and their global climate imprint. Rev. Geophys. 42, 1–43. https://doi.org/10.1029/2003RG000128.

Holzheimer, M., Sinninghe Damsté, J.S., Schouten, S., Havenith, R.W., Cunha, A.V., Minnaard, A.J., 2021. Total synthesis of the alleged structure of crenarchaeol enables structure revision. Angew. Chem. Int. Ed. 60, 17504–17513. https://doi-org.proxy.library.uu.nl/10.1002/anie.202105384.

Hopmans, E.C., Weijers, J.W.H., Schefuss, E., Herfort, L., Sinninghe Damsté, J.S., Schouten, S., 2004. A novel proxy for terrestrial organic matter in sediments based on branched and isoprenoid tetraether lipids. Earth Planet Sci. Lett. 224, 107–116. https://doi.org/10.1016/j.epsl.2004.05.012.

Hopmans, E.C., Schouten, S., Sinninghe Damsté, J.S., 2016. The effect of improved chromatography on GDGT-based palaeoproxies. Org. Geochem. 93, 1–6. https://doi.org/10.1016/j.orggeochem.2015.12.006.

IPCC, 2021. AR6 Synthesis Report: Climate Change 2022. Contribution of the Three Working Groups Assessment Reports, the Three Special Reports and the Synthesis Report to the Sixth Assessment Cycle of the Intergovernmental Panel on Climate Change. Cambridge University Press, Cambridge, United Kingdom and New York, NY, USA.

Li, F., Zhang, C.L., Wang, S., Chen, Y., Sun, C., Dong, H., Li, W., Klotz, M.G., Hedlund, B.P., 2014. Production of branched tetraether lipids in Tibetan hot springs: a possible linkage to nitrite reduction by thermotolerant or thermophilic bacteria? Chem. Geol. 386, 209–217. https://doi.org/10.1016/j.chemgeo.2014.08.015.

Loomis, S.E., Russell, J.M., Sinninghe Damsté, J.S., 2011. Distributions of branched GDGTs in soils and lake sediments from western Uganda: implications for a lacustrine paleothermometer. Org. Geochem. 42, 739–751. https://doi.org/10.1016/j.orggeochem.2011.06.004.

Loomis, S.E., Russell, J.M., Ladd, B., Street-Perrott, F.A., Sinninghe Damsté, J.S., 2012. Calibration and application of the branched GDGT temperature proxy on East African lake sediments. Earth Planet Sci. Lett. 357–358, 277–288. https://doi.org/10.1016/j.epsl.2012.09.031.

Loomis, S.E., Russell, J.M., Eggermont, H., Verschuren, D., Sinninghe Damsté, J.S., 2014a. Effects of temperature, pH and nutrient concentration on branched GDGT distributions in East African lakes: implications for paleoenvironmental reconstruction. Org. Geochem. 66, 25–37. https://doi.org/10.1016/j.orggeochem.2013.10.012.

Loomis, S.E., Russell, J.M., Heureux, A.M., D'Andrea, W.J., Sinninghe Damste, J.S.,

2014b. Seasonal variability of branched glycerol dialkyl glycerol tetraethers (brGDGTs) in a temperate lake system. Geochem. Cosmochim. Acta 144, 173–187. https://doi.org/10.1016/j.gca.2014.08.027.
Martin, C., Ménot, G., Thouveny, N., Davtian, N., Andrieu-Ponel, V., Reille, M., Bard, E., 2019. Impact of human activities and vegetation changes on the tetraether sources in Lake St Front (Massif Central, France). Org. Geochem. 135, 38–52. https://doi.org/10.1016/j.orggeochem.2019.06.005.
Martin, C., Ménot, G., Thouveny, N., Peyron, O., Andrieu-Ponel, V., Montade, V., Davtian, N., Reille, M., Bard, E., 2020. Early Holocene thermal maximum recorded by branched tetraethers and pollen in western Europe (massif central, France). Quat. Sci. Rev. 228, 106109. https://doi.org/10.1016/j.quascirev.2019.106109.
Martínez-Sosa, P., Tierney, J.E., Stefanescu, I.C., Dearing Crampton-Flood, E., Shuman, B.N., Routson, C., 2021. A global Bayesian temperature calibration for lacustrine brGDGTs. Geochem. Cosmochim. Acta 305, 87–105. https://doi.org/10.1016/j.gca.2021.04.038.
Menéndez Amor, J., Florschütz, F., 1962. Un aspect de la végétation en Espagne méridionale durant la dernière glaciation et l'Holocène. Geol. Mijnbouw 41, 131–134.
Menéndez Amor, J., Florschütz, F., 1964. Results of the preliminary palynological investigation of samples from a 50 m boring in southern Spain. Boletín de la Real Sociedad Española de Historia Natural Sección Biológica y Geológica 62, 251–255.
Morcillo-Montalbá, L., Rodrigo-Gámiz, M., Martínez-Ruiz, M., Ortega-Huertas, M., Schouten, S., Sinninghe Damsté, J.S., 2021. Rapid climate changes in the westernmost Mediterranean (Alboran Sea) over the last 35 kyr: new insights from four lipid paleothermometers ($U^{K'}_{37}$, TEX^{H}_{86}, RI-OH' and LDI). Paleoceanogr. Paleoclimatol. 36, e2020PA004171. https://doi.org/10.1029/2020PA004171.
Naafs, B.D.A., Gallego-Sala, A.V., Inglis, G.N., Pancost, R.D., 2017a. Refining the global branched glycerol dialkyl glycerol tetraether (brGDGT) soil temperature calibration. Org. Geochem. 106, 48–56 https://doi.org/10.1016/j.orggeochem.2017.01.009.
Naafs, B.D.A., Inglis, G.N., Zheng, Y., Amesbury, M.J., Biester, H., Bindler, R., Blewett, J., Burrows, M.A., del Castillo Torres, D., Chambers, F.M., Cohen, A.D., Evershed, R.P., Feakins, S.J., Gałka, M., Gallego-Sala, A., Gandois, L., Gray, D.M., Hatcher, P.G., Honorio Coronado, E.N., Hughes, P.D.M., Huguet, A., Könönen, M., Laggoun-Défarge, F., Lähteenoja, O., Lamentowicz, M., Marchant, R., McClymont, E., Pontevedra-Pombal, X., Ponton, C., Pourmand, A., Rizzuti, A.M., Rochefort, L., Schellekens, J., De Vleeschouwer, F., Pancost, R.D., 2017b. Introducing global peat-specific temperature and pH calibrations based on brGDGT bacterial lipids. Geochem. Cosmochim. Acta 208, 285–301. https://doi.org/10.1016/j.gca.2017.01.038.
Naughton, F., Sanchez Goñi, M.F., Rodrigues, T., Salgueiro, E., Costas, S., Desprat, S., Duprat, J., Michel, E., Rossignol, L., Zaragosi, S., Voelker, A.H.L., Abrantes, F., 2016. Climate variability across the last deglaciation in NW Iberia and its margin. Quat. Int. 414, 9–22. https://doi.org/10.1016/j.quaint.2015.08.073.
Niemann, H., Stadnitskaia, A., Wirth, S.B., Gilli, A., Anselmetti, F.S., Sinninghe Damsté, J.S., Schouten, S., Hopmans, E.C., Lehmann, M.F., 2012. Bacterial GDGTs in Holocene sediments and catchment soils of a high-alpine lake: application of the MBT/CBT-paleothermometer. Clim. Past 8, 889–906. https://doi.org/10.5194/cp-8-889-2012.
Ortiz, J.E., Torres, T., Delgado, A., Juliá, R., Lucini, M., Llamas, F.J., Resyes, E., Soler, V., Valle, M., 2004. The palaeoenvironmental and palaeohydrological evolution of Padul Peat Bog (Granada, Spain) over one million years, from elemental, isotopic and molecular geochemical proxies. Org. Geochem. 35, 1243–1260. https://doi.org/10.1016/j.orggeochem.2004.05.013.
Ortiz, J.E., Torres, T., Delgado, A., Llamas, J.F., Soler, V., Valle, M., Julià, R., Moreno, L., Díaz-Bautista, A., 2010. Palaeoenvironmental changes in the Padul Basin (Granada, Spain) over the last 1 Ma based on the biomarker content. Palaeogeogr. Palaeoclimatol. Palaeoecol. 298, 286–299.
Pancost, R.D., Hopmans, E.C., Sinninghe Damsté, J.S., Medinauth Shipboard Scientific Party, 2001. Archaeal lipids in Mediterranean cold seeps: molecular proxies for anaerobic methane oxidation. Geochem. Cosmochim. Acta 65, 1611–1627 https://doi.org/10.1016/S0016-7037(00)00562-7.
Peterse, F., Nicol, G.W., Schouten, S., Sinninghe Damsté, J.S., 2010. Influence of soil pH on the abundance and distribution of core and intact polar lipid-derived branched GDGTs in soil. Org. Geochem. 41, 1171–1175. https://doi.org/10.1016/j.orggeochem.2010.07.004.
Peterse, F., van der Meer, J., Schouten, S., Weijers, J.W.H., Fierer, N., Jackson, R.B., Kim, J.-K., Sinninghe Damsté, J.S., 2012. Revised calibration of the MBT-CBT paleotemperature proxy based on branched tetraether membrane lipids in surface soils. Geochem. Cosmochim. Acta 96, 215–229. https://doi.org/10.1016/j.gca.2012.08.011.
Pons, A., Reille, M., 1988. The Holocene and upper Pleistocene pollen record from Padul (Granada, Spain): a new study. Palaeogeogr. Palaeoclimatol. Palaeoecol. 66, 243–263. https://doi.org/10.1016/0031-0182(88)90202-7.
Powers, L.A., Johnson, T.C., Werne, J.P., Castañeda, I.S., Hopmans, E.C., Sinninghe Damsté, J.S., Schouten, S., 2005. Large temperature variability in the southern african tropics since the last glacial maximum. Geophys. Res. Lett. 32, L08706. https://doi.org/10.1029/2004GL022014.
Ramos-Román, M.J., Jiménez-Moreno, G., Camuera, J., García-Alix, A., Anderson, R.S., Jiménez-Espejo, F.J., Carrión, J.S., 2018a. Holocene climate aridification trend and human impact interrupted by millennial- and centennial-scale climate fluctuations from a new sedimentary record from Padul (Sierra Nevada, southern Iberian Peninsula). Clim. Past 14, 117–137. https://doi.org/10.5194/cp-14-117-2018.
Ramos-Román, M.J., Jiménez-Moreno, G., Camuera, J., García-Alix, A., Anderson, R.S., Jiménez-Espejo, F.J., Sachse, D., Toney, J., Carrión, J.S., Webster, C., Yanes, Y., 2018b. Millennial-scale cyclical environment and climate variability during the Holocene in the western Mediterranean region deduced from a new multiproxy analysis from the Padul record (Sierra Nevada, Spain). Global Planet. Change 168, 35–53. https://doi.org/10.1016/j.gloplacha.2018.06.003.
Rach, O., Hadeen, X., Sachse, D., 2020. An automated solid phase extraction procedure for lipid biomarker purification and stable isotope analysis. Org. Geochem. 142, 103995. https://doi.org/10.1016/j.orggeochem.2020.103995.
Rodrigo-Gámiz, M., Martínez-Ruiz, F., Jiménez-Espejo, F.J., Gallego-Torres, D., Nieto-Moreno, V., Romero, O., Ariztegui, D., 2011. Impact of climate variability in the western Mediterranean during the last 20,000 years: oceanic and atmospheric responses. Quat. Sci. Rev. 30, 2018–2034. https://doi.org/10.1016/j.quascirev.2011.05.011.
Rogerson, M., Cacho, I., Jiménez-Espejo, F., Reguera, M.I., Sierro, F.J., Martínez-Ruiz, F., Frigola, J., Canals, M., 2008. A dynamic explanation for the origin of the western Mediterranean organic-rich layers. G-cubed 9, Q07U01. https://doi.org/10.1029/2007GC001936.
Russell, J.M., Hopmans, E.C., Loomis, S.E., Liang, J., Sinninghe Damsté, J.S., 2018. Distributions of 5- and 6-methyl branched glycerol dialkyl glycerol tetraethers (brGDGTs) in East African lake sediment: effects of temperature, pH, and new lacustrine paleotemperature calibrations. Org. Geochem. 117, 56–69. https://doi.org/10.1016/j.orggeochem.2017.12.003.
Schouten, S., Huguet, C., Hopmans, E.C., Kienhuis, M.V.M., Sinninghe Damsté, J.S., 2007. Analytical methodology for TEX_{86} paleothermometry by high-performance liquid chromatography/atmospheric pressure chemical ionization-mass spectrometry. Anal. Chem. 79, 2940–2944. https://doi: 10.1021/ac062339v.
Schouten, S., Hopmans, E.C., Sinninghe Damsté, J.S., 2013. The organic geochemistry of glycerol dialkyl glycerol tetraether lipids: a review. Org. Geochem. 54, 19–61 https://doi.org/10.1016/j.orggeochem.2012.09.006.
Shakun, J.D., Clark, P.U., He, F., Marcott, S.A., Mix, A.C., Liu, Z., Otto-Bliesner, B., Schmittner, A., Bard, E., 2012. Global warming preceded by increasing carbon dioxide concentrations during the last deglaciation. Nature 484, 49–53. https://doi.org/10.1038/nature10915.
Sinninghe Damsté, J.S., Hopmans, E.C., Pancost, R.D., Schouten, S., Geenevasen, J.A.J., 2000. Newly discovered non-isoprenoid dialkyl diglycerol tetraether lipids in sediments. J. Chem. Soc., Chem. Commun. 23, 1683–1684.
Sinninghe Damsté, J.S., Rijpstra, W.I.C., Hopmans, E.C., Jung, M.Y., Kim, J.G., Rhee, S.K., Stieglmeier, M., Schleper, C., 2012. Intact polar and core glycerol dibiphytanyl glycerol tetraether lipids of group I.1a and I.1b Thaumarchaeota in soil. Appl. Environ. Microbiol. 78, 6866–6874. https://doi.org/10.1128/AEM.01681-12.
Sinninghe Damsté, J.S., Rijpstra, W.I.C., Foesel, B.U., Huber, K.J., Overmann, J., Nakagawa, S., Kim, J.J., Dunfield, P.F., Dedysh, S.N., Villanueva, L., 2018. An overview of the occurrence of ether-and ester-linked iso-diabolic acid membrane lipids in microbial cultures of the *Acidobacteria*: implications for brGDGT paleoproxies for temperature and pH. Org. Geochem. 124, 63–76. https://doi.org/10.1016/j.orggeochem.2018.07.006.
Sinninghe Damsté, J.S., Weber, Y., Zopfi, J., Lehmann, M.F., Niemann, H., 2022. Distributions and sources of isoprenoidal GDGTs in Lake Lugano and other central European (peri-) alpine lakes: lessons for their use as paleotemperature proxies. Quat. Sci. Rev. 277, 107352. https://doi.org/10.1016/j.quascirev.2021.107352.
Svensson, A., Andersen, K.K., Bigler, M., Clausen, H.B., Dahl-Jensen, D., Davies, S.M., Johnsen, S.J., Muscheler, R., Parrenin, F., Rasmussen, S.O., Röthlisberger, R., Seierstad, I., Steffensen, J.P., Vinther, B.M., 2008. A 60,000-year Greenland stratigraphic ice core chronology. Clim. Past 4, 47–57. https://doi.org/10.5194/cp-4-47-2008.
Tierney, J.E., Russell, J.M., 2009. Distributions of branched GDGTs in a tropical lake system: implications for lacustrine application of the MBT/CBT paleoproxy. Org. Geochem. 40, 1032–1036. https://doi.org/10.1016/j.orggeochem.2009.04.014.
Tierney, J.E., Russell, J.M., Eggermont, H., Hopmans, E., Verschuren, D., Sinninghe Damsté, J.S., 2010. Environmental controls on branched tetraether lipid distributions in tropical East African lake sediments. Geochem. Cosmochim. Acta 74, 4902–4918. https://doi.org/10.1016/j.gca.2010.06.002.
Toucanne, S., Minto'o, C.M.A., Fontanier, C., Bassetti, M.A., Jorry, S.J., Jouet, G., 2015. Tracking rainfall in the northern Mediterranean borderlands during sapropel deposition. Quat. Sci. Rev. 129, 178–195. https://doi.org/10.1016/j.quascirev.2015.10.016.
van Bree, L.G.J., Peterse, F., Baxter, A.J., De Crop, W., van Grinsven, S., Villanueva, L., Verschuren, D., Sinninghe Damsté, J.S., 2020. Seasonal variability and sources of in situ brGDGT production in a permanently stratified African crater lake. Biogeosciences 17, 5443–5463. https://doi.org/10.5194/bg-17-5443-2020.
Warden, L., Kim, J.-H., Zell, C., Vis, G.-J., de Stigter, H., Bonnin, J., Sinninghe Damsté, J.S., 2016. Examining the provenance of branched GDGTs in the Tagus River drainage basin and its outflow into the Atlantic Ocean over the Holocene to determine their usefulness for paleoclimate applications. Biogeosciences 13, 5719–5738. https://doi.org/10.5194/bg-13-5719-2016.
Weber, Y., De Jonge, C., Rijpstra, W.I.C., Hopmans, E.C., Stadnitskaia, A., Schubert, C.J., Lehmann, M.F., Sinninghe Damsté, J.S., Niemann, H., 2015. Identification and carbon isotope composition of a novel branched GDGT isomer in lake sediments: evidence for lacustrine branched GDGT production. Geochem. Cosmochim. Acta 154, 118–129 https://doi.org/10.1016/j.gca.2015.01.032.
Weber, Y., Sinninghe Damsté, J.S., Zopfi, J., De Jonge, C., Gilli, A., Schubert, C.J.,

Lepori, F., Lehmann, M.F., Niemann, H., 2018. Redox-dependent niche differentiation provides evidence for multiple bacterial sources of glycerol tetraether lipids in lakes. Proc. Natl. Acad. Sci. U. S. A. 115 (43), 10926–10931. www.pnas.org/cgi/doi/10.1073/pnas.1805186115.

Webster, C.E., 2018. Late-Pleistocene and Holocene Record of Fire at Padul Peat Bog (Granada, Spain). MSc Thesis, Northern Arizona University, USA.

Weijers, J.W., Schouten, S., Spaargaren, O.C., Sinninghe Damsté, J.S., 2006. Occurrence and distribution of tetraether membrane lipids in soils: implications for the use of the TEX_{86} proxy and the BIT index. Org. Geochem. 37, 1680–1693 https://dx.doi.org/10.1016/j.orggeochem.2006.07.018.

Weijers, J.W.H., Schouten, S., van Den Donker, J.C., Hopmans, E.C., Sinninghe Damsté, J.S., 2007a. Environmental controls on bacterial tetraether membrane lipid distribution in soils. Geochem. Cosmochim. Acta 71, 703–713 https://dx.doi.org/10.1016/j.gca.2006.10.003.

Weijers, J.W.H., Schefuss, E., Schouten, S., Sinninghe Damsté, J.S., 2007b. Coupled thermal and hydrological evolution of tropical Africa over the last deglaciation. Science 315, 1701–1704 https://dx.doi.org/10.1126/science.1138131.

Woltering, M., Atahan, P., Grice, K., Heijnis, H., Taffs, K., Dodson, J., 2014. Glacial and Holocene terrestrial temperature variability in subtropical east Australia as inferred from branched GDGT distributions in a sediment core from Lake McKenzie. Quaternary Research 82 (1), 132–145. https://doi.org/10.1016/j.yqres.2014.02.005.

Zell, C., Kim, J.-H., Hollander, D., Lorenzoni, L., Baker, P., Silva, C., Nittrouer, C., Sinninghe Damsté, J.S., 2014. Sources and distribution of branched and isoprenoid tetraether lipids on the Amazon shelf and fan: implications for the use of GDGT-based paleothermometers in marine sediments. Geochem. Cosmochim. Acta 139, 293–312. https://doi.org/10.1016/j.gca.2014.04.038.

Zhang, Z.-X., Li, J., Chen, Z., Sun, Z., Yang, H., Fu, M., Peng, X., 2020. The effect of methane seeps on the bacterial tetraether lipid distributions at the Okinawa Trough. Mar. Chem. 225, 103845. https://doi.org/10.1016/j.marchem.2020.103845.

Zhang, C., Zhao, C., Zhou, A., Zhang, H., Liu, W., Feng, X., Sun, X., Yan, T., Leng, C., Shen, J., Chen, F., 2021. Quantification of temperature and precipitation changes in northern China during the "5000-year" Chinese History. Quat. Sci. Rev. 255, 106819. https://doi.org/10.1016/j.quascirev.2021.1068.

Zhao, C., Rohling, E.J., Liu, Z., Yang, X., Zhang, E., Cheng, J., Liu, Z., An, Z., Yang, X., Feng, X., Sun, X., Zhang, C., Yan, T., Long, H., Yan, H., Yu, Z., Liu, W., Yum, S.-Y., Shen, J., 2021. Possible obliquity-forced warmth in southern Asia during the last glacial stage. Sci. Bull. 66, 1136–1145. https://doi.org/10.1016/j.scib.2020.11.016.